Upon solving

$$\Delta J_{ad}=(V_{13}V_{22}-V_{23}V_{12})/\Delta \quad \text{(A32)}$$

and

$$\Delta J_{aa}=(V_{11}V_{23}-V_{12}V_{13})/\Delta, \quad \text{(A33)}$$

where

$$\Delta=V_{11}V_{22}-V_{12}^2, \quad \text{(A34)}$$

the new J_{ad}' and J_{aa}' can be found to be

$$J_{ad}'=J_{ad}+\Delta J_{ad} \quad \text{(A35)}$$

and

$$J_{aa}'=J_{aa}+\Delta J_{aa}. \quad \text{(A36)}$$

The process is repeated until the curve is fitted to the desired accuracy.

PHYSICAL REVIEW VOLUME 175, NUMBER 2 10 NOVEMBER 1968

de Haas–van Alphen Effect in Antiferromagnetic Chromium*

J. E. GRAEBNER†‡ AND J. A. MARCUS
Northwestern University, Evanston, Illinois

(Received 22 May 1968)

de Haas–van Alphen torque oscillations have been studied in single-domain crystals of Cr in magnetic fields to 33 kG and have been analyzed by computer calculation of their Fourier transform. Extensive data in all major symmetry planes and several nonsymmetry planes confirm the tetragonal symmetry of the Fermi surface in the antiferromagnetic state. The frequency resolution is sufficient to isolate several families of data, a number of which can be represented well by simple geometrical Fermi-surface models. Band calculations for paramagnetic Cr indicate a Fermi surface which contains a closed hole sheet at the point N of the Brillouin zone and a closed electron sheet located along ΓH. For simplicity, it is assumed that the electron and hole octahedra at Γ and H, respectively, are destroyed by the interaction which stabilizes the antiferromagnetic state. The surviving Fermi-surface sheets at N and along ΓH are truncated by energy gaps due to the antiferromagnetic Q vector, as proposed by Lomer. Several of the resulting surfaces resemble those obtained from the geometrical analysis of the data. By adjusting the dimensions and shape of the hole surfaces at N, it is possible to interpret three families of data with an accuracy of $\sim$10% in area. Applying a similar procedure to the electron surface along ΓH yields $\sim$20% agreement with a fourth family of data. The many remaining frequencies receive either a tentative assignment or none at all.

I. INTRODUCTION

THE antiferromagnetic structure in Cr is known[1–7] to have a periodicity which is different from that of the lattice. The antiferromagnetic arrangement of spins includes a long-wavelength amplitude modulation producing a characteristic wave vector Q which is incommensurate with the lattice: $\mathbf{Q}=(2\pi/a)(1-\delta, 0, 0)$, where a is the lattice constant, and $\delta\approx 0.04$ at liquid-helium temperatures. The structure has been interpreted[8–14] as a linearly polarized spin-density wave (SDW) which is stabilized by an interaction between parallel faces of the Fermi surface separated from each other by Q. It has been suggested[15] that this additional periodic structure, or superlattice, has a truncating effect on the Fermi surface, analogous to the introduction of Brillouin-zone boundaries by the ordinary lattice. The effects of these truncations on the paramagnetic Fermi surface should be observable in the de Haas–van Alphen (dHvA) effect.

One would expect the magnetic symmetry of a single crystal of Cr to be tetragonal if it contained a single SDW (single Q). The experimental observation of

* Supported by the National Science Foundation and the Advanced Research Projects Agency of the Department of Defense.

† Work performed in partial fulfillment of the requirements for the Ph.D. degree, Northwestern University, Evanston, Ill.

‡ Present address: Bell Telephone Laboratories, Murray Hill, N.J. 07971.

[1] C. G. Shull and M. K. Wilkinson, Rev. Mod. Phys. **25**, 100 (1953).

[2] L. Corliss, J. Hastings, and R. Weiss, Phys. Rev. Letters **3**, 211 (1959).

[3] M. K. Wilkinson, E. O. Wollan, W. C. Koehler, and J. W. Cable, Phys. Rev. **127**, 2080 (1962).

[4] V. N. Bykov, V. S. Golovkin, N. V. Ageev, V. A. Levdik and S. I. Vinogradov, Dokl. Akad. Nauk SSSR **128**, 1153 (1959) [English transl.: Soviet Phys.—Doklady **4**, 1070 (1959)].

[5] J. M. Hastings, reported at the Conference on Neutron Diffraction at Gatlinburg, Tennessee, 1960 (unpublished).

[6] G. E. Bacon, Acta Cryst. **14**, 823 (1961).

[7] G. Shirane and W. J. Takei, J. Phys. Soc. Japan **17**, Suppl. B-III, 35 (1962).

[8] W. M. Lomer, Proc. Phys. Soc. (London) **80**, 489 (1962); **84**, 327 (1964).

[9] A. W. Overhauser, Phys. Rev. **128**, 1437 (1962).

[10] W. Kohn and S. J. Nettel, Phys. Rev. Letters **5**, 8 (1960).

[11] Peter A. Fedders and Paul C. Martin, Phys. Rev. **143**, 143 (1966).

[12] L. M. Falicov and M. J. Zuckermann, Phys. Rev. **160**, 372 (1967).

[13] C. Herring, in *Magnetism*, edited by G. T. Rado and H. Suhl (Academic Press Inc., New York, 1966), Vol. IV.

[14] A. Arrott, in *Magnetism*, edited by G. T. Rado and H. Suhl (Academic Press Inc., New York, 1966), Vol. IIB.

[15] W. M. Lomer, in *Proceedings of the International Conference on Magnetism, Nottingham, 1964* (The Institute of Physics and The Physical Society, London, 1965), p. 127.

magnetic symmetry lower than tetragonal has been ascribed to a domain structure. It was discovered[16] in magnetic-susceptibility measurements that the magnetic state of the crystal depends on the magnetic field $\mathbf{H}_c$ present when the crystal is cooled through the Néel temperature T_N (38.5°C). Subsequently, neutron-diffraction investigation[17–19] of crystals treated in this way showed that for $\mathbf{H}_c > \sim 20$ kG along a ⟨100⟩ direction, the magnetic structure could be described by a single **Q**, parallel to $\mathbf{H}_c$, while for $\mathbf{H}_c = 0$ there are three **Q**'s, one along each ⟨100⟩ direction. Because the neutron beam intercepted the entire crystal, interpretation of the triple-**Q** state was ambiguous. The state might arise in either of two ways: (a) The crystal might be subdivided into domains, each containing a single SDW along a particular ⟨100⟩ direction, with a random distribution of domains among the three ⟨100⟩ directions, or (b) the crystal might contain three interpenetrating SDW's which coexist throughout the entire volume. The initial dHvA data[20] of the present investigation ruled out the interpenetrating SDW model. The dHvA data of the triple-**Q** state were found to be a simple superposition of three sets of the tetragonal (single-**Q**) data,[21] with the three tetrad axes directed along the three ⟨100⟩ directions. This result rules out the interpenetrating SDW model because some entirely new frequencies would be expected if two or three SDW's truncated the same Fermi surface. It is, however, consistent with the domain model, since the Fermi surface in each domain would always be truncated by only a single SDW.

dHvA data are presented below for the single-**Q** state only. No new Fermi-surface information was found in the triple-**Q** state.

In Sec. II the apparatus and data reduction are described. The reduced data are presented in Sec. III. The interpretation is carried out in two stages: In Sec. IV A, simple ellipsoidal and cylindrical models are fitted quantitatively to several families of data; then in Sec. IV B, a theoretical model for the paramagnetic Fermi surface is perturbed by the antiferromagnetic superlattice, and the resulting sheets are examined for surfaces suggested by the geometrical models. In Sec. IV B, we assume that both first- and second-order energy gaps are important, as indicated by recent calculations.[12]

II. EXPERIMENT

The dHvA torque oscillations were measured with a Condon torsion balance[22] and an 11-in. iron-core electromagnet with maximum field of 33 kG. A conventional double Dewar and pumping system provided temperatures to 1.25°K.

The bulk of the data was taken on four samples with masses in the range 30–60 mg. The crystals, of irregular shape, were cut from larger, carefully selected samples of Batelle iodide-vapor-process chromium with residual resistance ratios of 1000–1200. After electropolishing, the crystals were oriented with an accuracy of ±0.2° and attached with a small spot of epoxy to the quartz rod of the torsion balance. (Duco cement was also used and produced no noticeable difference in the effect of field cooling.) Field cooling consisted of heating the crystal to ~70°C in the Dewar, turning up the magnetic field $\mathbf{H}_c$ to 33 kG along a ⟨100⟩ direction, and allowing the crystal to cool slowly (~40 min) to 77°K before turning off the field. The precaution of turning off the field before passing through the spin-flip temperature (120°K) to avoid flipping[23] the **Q** was found to be unnecessary at these relatively low fields. Also, various values of H_c were investigated[20]: $H_c < \sim 20$ kG produced a multi-**Q** state, while for $H_c > \sim 20$ kG the dHvA data showed that 98±2% of the volume of the crystal was in a single-**Q** state.

The oscillatory torque was recorded as a direct function of $1/H$ on a Moseley 2S x-y recorder specially equipped with a rotary digital encoder for each axis. A Hall dividing circuit[24] with a Bell BH701 Hall probe supplied the $1/H$ signal. The readings of the encoders were recorded automatically on a Precision Instrument 1167 incremental magnetic tape recorder for later computer analysis. The resolution of each encoder was 1/1000 of full scale, so that usually 1000 x-y pairs of numbers were recorded for each field sweep.

The Fourier transform of each field sweep was calculated on a CDC 3400 computer after adjusting the data to improve the resolution and to correct for certain instrumental nonlinearities.[25] (a) To minimize the broadening of Fourier transform peaks that would be caused by the usual exponential growth of oscillation amplitude with magnetic field strength, the torque scale at low fields was expanded by the computer to

[16] R. A. Montalvo and J. A. Marcus, Phys. Letters **8,** 151 (1964); see also W. M. Lomer and J. A. Marcus, in *Proceedings of the International Conference on Magnetism, Nottingham, 1964* (The Institute of Physics and The Physical Society, London, 1965), p. 201.

[17] A. Arrott, S. A. Werner, and H. Kendrick, Phys. Rev. Letters **14,** 1022 (1965).

[18] T. J. Bastow and R. Street, Phys. Rev. **141,** 510 (1966); see also R. Street, J. Appl. Phys. **39,** 1050 (1968).

[19] S. A. Werner, A. Arrott, and H. Kendrick, Phys. Rev. **155,** 528 (1967).

[20] J. Graebner and J. A. Marcus, J. Appl. Phys. **37,** 1262 (1966).

[21] B. R. Watts, Phys. Letters **10,** 275 (1964); and in *Low Temperature Physics* (Plenum Press, Inc., New York, 1965), Vol. 9, p. 779. Watts observed in pulsed-field dHvA measurements that for large $\mathbf{H}_c$ the Fermi surface is completely tetragonal, and he concluded that a large $\mathbf{H}_c$ produces a single tetragonal domain. Conclusions about the state produced by $\mathbf{H}_c = 0$ had to be tentative because the large measuring field had a reorienting effect on the magnetic structure and prevented clear observation of the triple-**Q** state. Also, the possibility of an interpenetrating SDW state was not considered.

[22] J. H. Condon and J. A. Marcus, Phys. Rev. **134,** A446 (1964).

[23] A. J. Arko, J. A. Marcus, and W. A. Reed, Phys. Letters **23,** 617 (1966); and Phys. Rev. (to be published).

[24] R. J. Higgins, Rev. Sci. Instr. **36,** 1536 (1965).

[25] For a more detailed discussion, see J. E. Graebner, thesis, Northwestern University, 1968 (unpublished).

make the oscillation amplitude roughly constant. (b) The $1/H$ scale was corrected for slight nonlinearities in the Hall dividing circuit. Nonlinearity as small as $\frac{1}{2}$ wavelength of the frequency of interest could have caused severe distortion of the transform peak and put all the information of the central peak into sidebands. Deviations from linearity therefore had to be kept to a small fraction of one wavelength. A $1/H$ correction function was derived from a particular field sweep which was dominated by a single frequency (see below). The oscillations were assumed to be exactly periodic in $1/H$ and the calculated deviations were taken as the $1/H$ correction function. (The assumption of exact periodicity in $1/H$ was checked over the range 25–33 kG with a Rawson rotating-coil flux meter and was found to be valid within the accuracy of the measurement, ~10 G.) The maximum correction for nonlinearity in a typical field sweep from 300 to 395×10^{-7} G^{-1} was 0.1×10^{-7} G^{-1}, or 0.25% of full scale. The corrections were more significant for longer field sweeps and lower field regions. (c) The data were often filtered electronically and/or digitally to suppress low or high frequencies. Filtering against very low frequencies eliminated the rapidly rising baseline due to the monotonic torque. When analyzing for medium or low frequencies, suppression of high frequencies saved computer time by reducing the number of points required to define the data uniquely.

If the N points in a field sweep are labeled $g(x_n)$, where $x=1/H$, the Fourier transform as a function of discrete frequency f_m can be written

$$G(f_m)=\sum_{n=1}^{N} g(x_n)\,\exp(i2\pi f_m x_n)\,\Delta x_n. \qquad (1)$$

The magnitude of $G(f_m)$ was calculated for successive values of f_m over the frequency range of interest and plotted versus frequency on an off-line Calcomp plotter. A number of time-saving features were employed in the calculation, especially where high accuracy was unnecessary.[25,26] Calculations of sine and cosine, for example, were eliminated by precalculating 1000 values for each between 0 and 2π and storing them as a table in memory.

The magnitude of the Fourier transform for a simple sinusoidal wave $g(x)=A\sin2\pi f_0 x$ of finite length L is $|G(f)|=\frac{1}{2}AL\,(\sin\alpha)/\alpha$, where $\alpha=\pi L(f-f_0)$. The central peak at $f=f_0$ has a full width at half-maximum of $\delta f\simeq 1/L$. The width of the peak at half-maximum, i.e., the resolution, is therefore independent of f_0 and is determined only by the length of the wavetrain. Subsidiary peaks (sidebands) occur at regularly spaced frequency intervals and decrease in amplitude as $1/|f-f_0|$. The amplitude of the first sideband is 22%

[26] An algorithm for fast computation of the Fourier transform [J. W. Cooley and J. W. Tukey, Math. Computation **19**, 297 (1965)] was published after this computer program was written but should make future reduction of dHvA data by computer even more attractive.

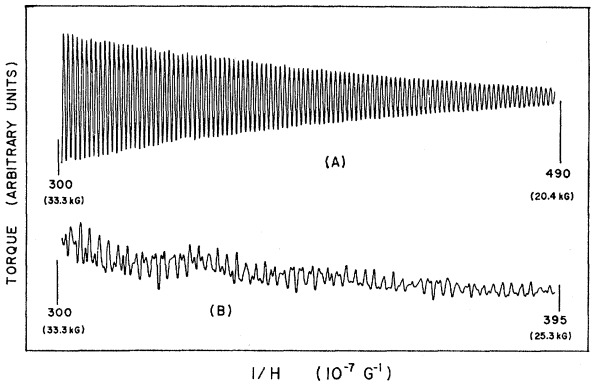

FIG. 1. dHvA torque oscillations in Cr, (a) for **H** within a few tenths of a degree of [010] and **Q** || [001], and (b) for a more general field direction. The slowly changing baseline in (b) is due to the monotonic torque (Ref. 16) and was subtracted before analysis.

that of the central peak, and the half-width of any sideband is one-half that of the central peak. The spacing Δf in the numerical analysis was chosen to provide several points per central peak, $\Delta f\lesssim\frac{1}{2}\delta f$.

dHvA frequencies greater than 10^6 G, which constituted the bulk of the data, were studied with field sweeps from ~25 to 33 kG ($300\text{–}395\times10^{-7}$ G^{-1}). Greater resolution by a factor of 2 was sometimes used by extending the range down to ~20 kG ($300\text{–}490\times10^{-7}$ G^{-1}). Figure 1 shows examples of both field ranges. The particularly simple field sweep, Fig. 1(a), is for **H** aligned within a few tenths of a degree of a ⟨100⟩ direction perpendicular to **Q** (see below, frequency ζ in plane C). A typical field sweep at a more general angle is shown in Fig. 1(b). The dominant oscillations in Fig. 1(a) were used to linearize the $1/H$ signal, as described above.

The Fourier transforms of these data are shown in Fig. 2. Figure 2(a) is dominated by a single frequency, as expected, and several weaker frequencies are also revealed. Figure 2(b) contains at least 14 peaks, and the peak half-width is close to the expected value, 0.1×10^6 G, determined from the range of $1/H$. The broader peaks at ~0.3 and $\sim13.5\times10^6$ G are due to pairs of very close frequencies which are not separated with this field sweep range. To save computer time, the higher resolution of Fig. 2(a) was used only when necessary.

The resolution illustrated in Fig. 2(b) is typical of most of the data to be presented. For midrange frequencies, $\sim10\times10^6$ G, two peaks separated by 1% are resolved, while the location of an isolated peak can be determined to ~0.2%. The latter figure represents the stability of the $1/H$ signal.

Figure 2 illustrates that sidebands were not a serious problem in interpreting the transforms. The fact that the sideband amplitudes were smaller than expected for simple sinusoidal data is thought to be due to amplitude and frequency modulation, which cause

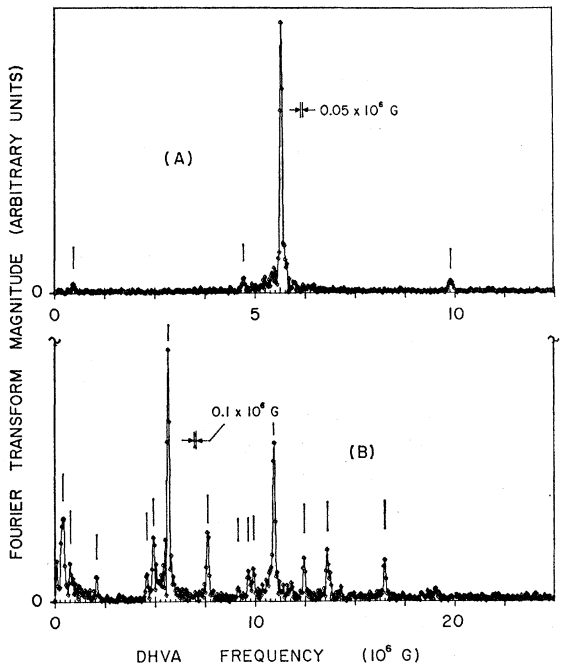

FIG. 2. Fourier-transform magnitudes, computed from the data of Fig. 1. The computed points (diamonds) are connected by straight lines. The expected half-widths of the peaks are indicated by arrows and differ from (a) to (b) because the $1/H$ ranges of the data differ. Note also the difference in frequency scales.

more destructive interference of sidebands than of the central peak. The corrections described above were not sufficient to convert the data into perfectly sinusoidal waves, leaving enough amplitude and frequency modulation to weaken the sidebands. Because the sidebands were not a problem, the usual device[27] of multiplying the data by $(\sin\beta)/\beta$, with $\beta=2\pi(x-\frac{1}{2}L)/L$, was not considered profitable. That procedure reduces the amplitude of the first sideband by a factor of ~ 4 at the expense of $\sim 50\%$ in resolution of the central peak.

III. RESULTS

In view of the complexity of the data, most measurements were made with **H** lying in crystallographic planes of high symmetry: {100}, {110}, and {111}. The degeneracies which often occur in such planes helped reduce the number of apparent frequencies and simplified the task of sorting the data. A few nonsymmetry planes were studied to resolve questions of degeneracy or connectivity.

Results for the major symmetry planes of the single-**Q** state are presented in Fig. 3. **Q** is parallel to [001]. Tetragonal symmetry imposed on a nominally cubic structure results in two inequivalent (100) planes (labeled C and D in the figure), two inequivalent (110) planes (B and E), and the (111) plane (A). We refer to plane D as the basal plane.

The dHvA data for Cr show tetragonal symmetry with the tetrad axis parallel to **Q**. This symmetry has been observed previously[20,21] and was discussed above in Sec. I. The present data are much more extensive than previous dHvA data for Cr,[20,21,28] and have sufficient resolution to justify a detailed interpretation. The present data show general agreement with the data of previous workers, to within the resolution of those measurements. A striking feature of the data is the limited angular range of most branches. For example, there are only two branches in plane C which are continuous from [001] to [100]. Another curious feature is the frequent appearance of pairs and even triplets of curves separated by only $\sim 0.3\times 10^6$ G. This is a well-resolved separation and is reproduced from sample to sample; furthermore, there is good continuity of the separated branches at points where the various planes intersect.

On first inspection, the frequencies of plane D labeled θ, λ, and π in Fig. 3 appear to be the second, third, and fourth harmonics of frequency ζ. More detailed analysis shows that this is not the case. In Fig. 4 the data points are shown together with solid lines which represent the true harmonics of ζ in planes A, B, and D. Frequency θ is clearly not a second harmonic. At [110] in plane D, frequency λ agrees well with the third harmonic but deviates from it as **H** is rotated away from [110]. This deviation is greater than the experimental uncertainty and is even more pronounced in planes A and B, which also intersect [110]. The data for π are weak but appear to deviate significantly from the fourth harmonic in plane A. When a similar comparison is made between π and σ and the second and third harmonics of θ, the agreement is even less favorable than in Fig. 4. Likewise, tests to determine whether various frequencies could be represented by sums or differences of other frequencies yielded negative results. Recent measurements[29] of ultrasonic attenuation in Cr indicate a richness of harmonics as well as sum and difference frequencies, the origin of which has not been established.

In the discussion which follows, most attention will be concentrated on those frequencies which can be followed through several symmetry planes. To ease the task of sorting the many branches into families, the data were plotted on a special three-dimensional grid. For tetragonal symmetry, all unique dHvA information is to be found with **H** lying in the $\frac{1}{16}\times 4\pi$ solid angle bounded by planes B, C, and D. The planes A–E can be folded together to form a three-dimensional array for such a half-quadrant. In order that the planes of data remain planar in the construction, they were first replotted according to a gnomonic projection of the magnetic-field direction. (The special feature of the

[27] See, e.g., C. Lanczos, *Applied Analysis* (Prentice Hall, Inc., Englewood Cliffs, N.J., 1964), p. 271.

[28] G. B. Brandt and J. A. Rayne, Phys. Rev. **132**, 1945 (1963).

[29] W. D. Wallace and H. V. Bohm, J. Phys. Chem. Solids **29**, 721 (1968).

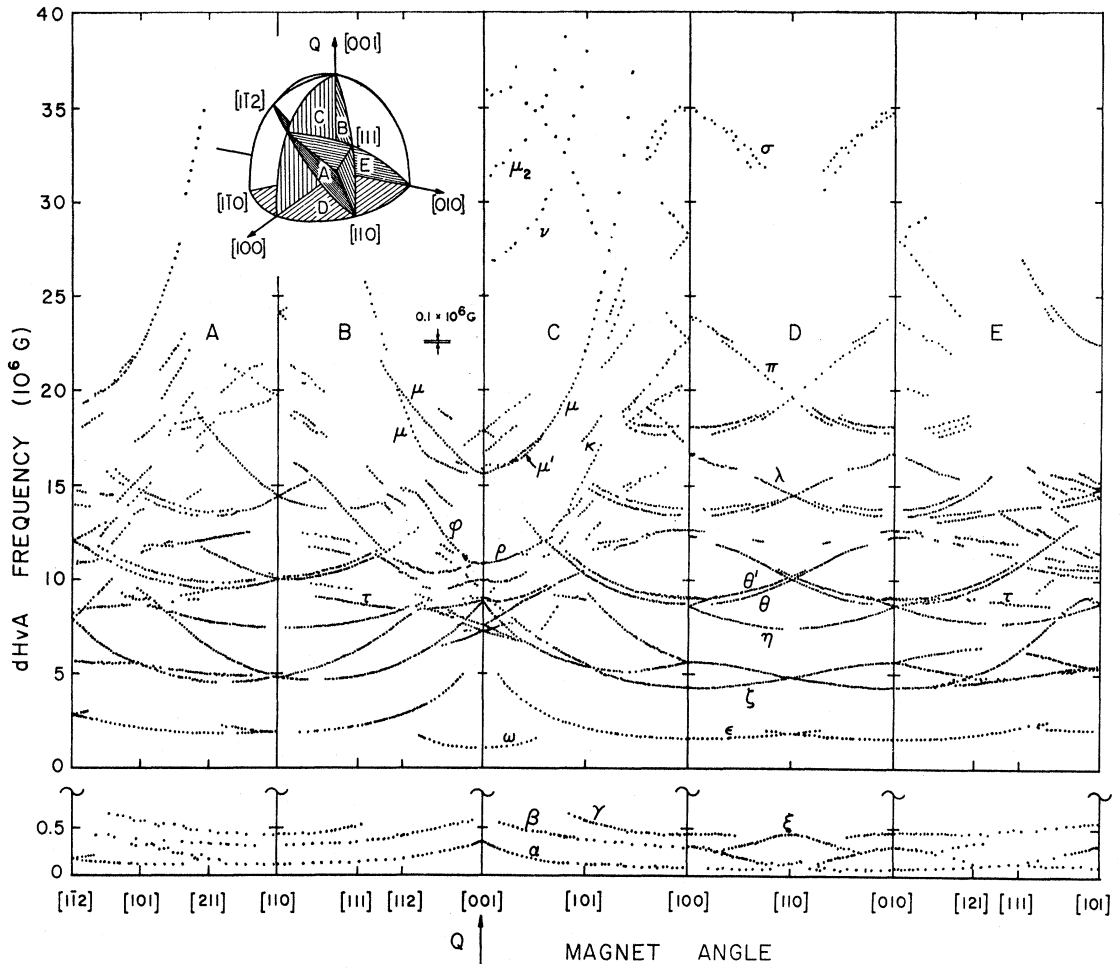

FIG. 3. dHvA frequency versus magnetic field direction for the major symmetry planes of Cr. The resolution shown by arrows is that of Fig. 2(b).

gnomonic projection is that any great circle is a straight line.) The data points of each plane were transferred to $\frac{1}{32}$-in. clear Plexiglas with the angle scale made suitably nonlinear (Fig. 5) and the planes were fitted together with the necessary folds and cuts. This frequency versus magnet-angle space was extremely useful in correlating the many short frequency branches. Nonsymmetry planes of data could also be inserted as planes in the construction, simplifying their interpretation.

Several details of connectivity are not obvious from the data of Fig. 3. Care was taken to distinguish the two families labeled η and θ. By use of long field sweeps (300–490×10^{-7} G^{-1}), it was established that η intersects the [100] direction with nonzero slope in the basal plane. Furthermore, both the weaker upper branch θ' as well as the stronger branch θ were found to have nonzero slope at [110] in the basal plane. This is indicated schematically in Fig. 6; branches 1 and 2 constitute η, 3 is θ, and 4 is θ'. To test the hypothesis that branch 2 extends only 15° or 20° from [100] and does not connect with branches 3 or 4, measurements were made in a nonsymmetry plane (Fig. 7) intersecting plane C at approximately right angles, 23° from [100], as indicated by the arrow in Fig. 6. At the point of intersection of the planes, branches 3 and 4 are high enough that the crossing of 1 and 2 and the limited angular range of 2 are clear. Also, the value of 1 and 2 at their crossing is the same as at [100], within ~1%. This equality suggests that the slope of η is very nearly zero between this point and [100], and would explain the absence of torque data in this region of plane C.

The three strong branches labeled μ in planes B and C of Fig. 3 are believed to intersect at [001], at a value 15.60×10^6 G. We note that the point of crossing of the two branches of μ in plane B at ~37° from [001] has the same coordinates (frequency and angle from [001]) as a point on the branch of μ in plane C. The equality supports the assumption that the three branches belong to the same family. The subsidiary branch μ' in plane C, which is distinguishable from the dominant μ through ~25° from [001], appears to cross μ and intersect [001] at a slightly higher value than μ, 16.0×10^6 G.

The high-frequency μ_2 in plane C is quite weak. It

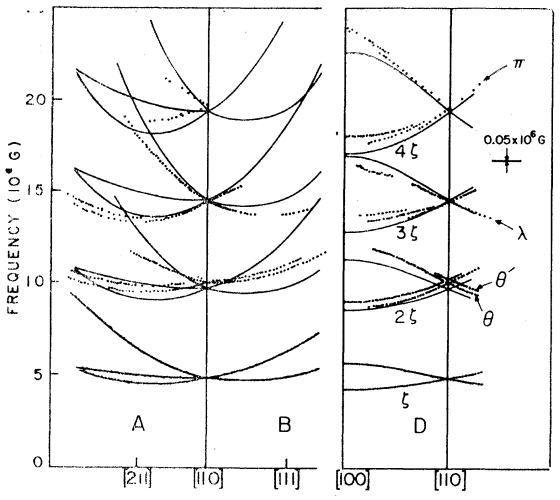

FIG. 4. Portions of Fig. 3 for comparison of frequencies θ, θ', λ, and π with the second, third, and fourth harmonics of ζ (represented by solid lines). The resolution shown by arrows is that of Fig. 2(a).

agrees with a line drawn at twice the frequency of μ (see below, Fig. 15) and is assumed to be a harmonic.

The field and temperature dependence of dHvA amplitudes was studied to determine effective masses (m^*/m_0) and Dingle temperatures[30] (T_D) for a few frequencies. Some results are listed in Table I. Short field sweeps, of length just sufficient to isolate a particular frequency from nearby frequencies, were taken at various temperatures and fields, and the amplitude of oscillation was measured directly from the height of the Fourier transform peak. The usual exponential approximation to the hyperbolic sine factor in the theoretical amplitude[31] gave less than a few percent error for the field, temperature, and masses encountered. Reliable values of T_D were difficult to obtain in the high symmetry planes because of the frequent appear-

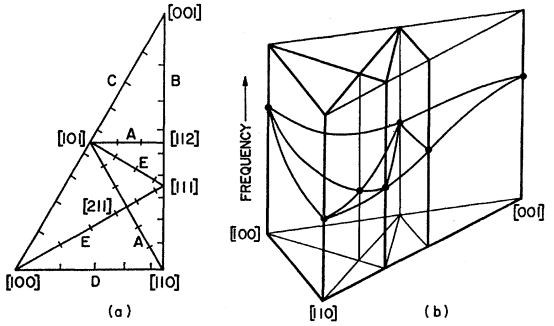

FIG. 5 (a) Gnomonic projection about [111] of the half-quadrant in which data were taken. Cross marks occur at 10° intervals between axes. (b) Device for three-dimensional display of the data in Fig. 3 (see text). A single sheet of data is indicated schematically by the curved lines.

[30] R. B. Dingle, Proc. Roy. Soc. (London) **A211**, 517 (1952).
[31] I. M. Lifshitz and A. M. Kosevich, Zh. Eksperim. i Teor. Fiz. **29**, 663 (1955) [English transl.: Soviet Phys—JETP **2**, 636 (1956)].

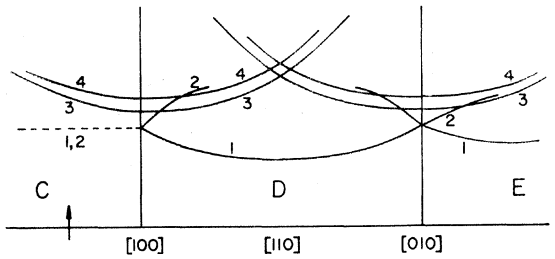

FIG. 6. Schematic diagram showing the connectivity of data families η (1 and 2), θ (3), and θ' (4).

ance of very-long-wavelength undulations in the amplitude-versus-field plots due, for example, to slight misorientation of the sample that lifts a twofold degeneracy and creates a long-wavelength beat.

The amplitude of the torque oscillations was inspected for anomalous dependence on field strength as evidence for magnetic breakdown.[12,15,23] No positive evidence was found, for the few frequencies investigated. Such effects may have been quite small, however, because of the limited field range used (~15–33 kG, a factor of ~2), and may have been masked by the slow undulations described above.

IV. INTERPRETATION

A. Geometrical Models

As a first step in interpreting the data, we consider the general types of data which would result from simple closed surfaces situated at various symmetry points in a tetragonal **k** space. This part of the analysis applies to any tetragonal system. Figure 8 shows the variation of extremal cross-sectional areas for families

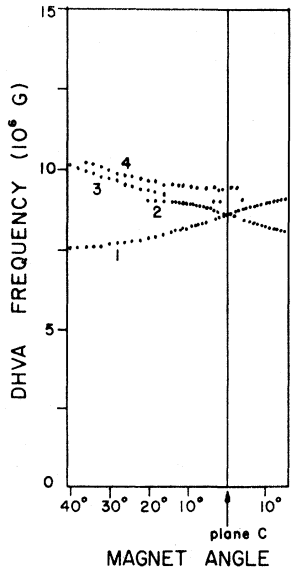

FIG. 7. Data in part of a nonsymmetry plane which intersects plane C at approximately right angles at the location of the arrow in Fig. 6.

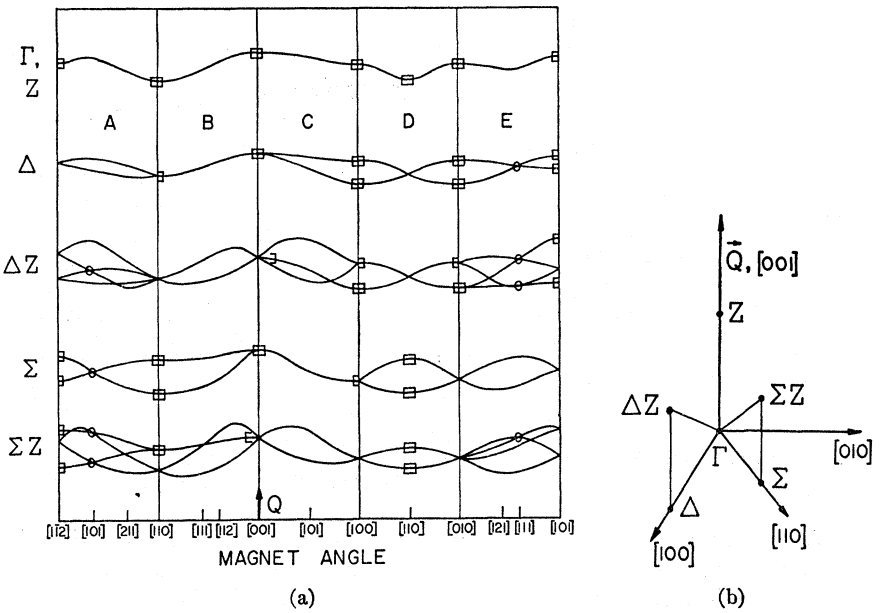

FIG. 8. (a) General types of dHvA data expected from families of simple closed surfaces located at the various symmetry points of a tetragonal **k** space. (b) The ordinate in (a) is dHvA frequency, and the magnetic field is rotated through the same planes as in Fig. 3. Each closed surface is assumed to support only a single extremal area and to possess only the symmetry of its site. A box or half-box on a frequency branch at or near a major symmetry direction indicates that the branch meets the axis with zero slope. A circle around the crossing of two branches near a major symmetry axis indicates that the crossing must occur at the axis. In (b), the points ΔZ and ΣZ are general points in the Δ-Z and Σ-Z planes, respectively.

of closed surfaces associated with each of the six general symmetry points considered[32]: Γ, Z, Σ, Δ, ΔZ, or ΣZ. **H** is allowed to rotate through the five planes of Fig. 3. (Watts[21] constructed a diagram similar to Fig. 8 but did not have sufficient data to perform the analysis.)

TABLE I. Values of m^*/m_0 and T_D, plane *C*.

Family of data	Angle from Q (deg)	Frequency (10^6G)	m^*/m_0	T_D (°K)
ϵ	65	1.7	0.18	0.47
ζ	3	8.3	0.39	0.5
	12.5	7.9	0.43	
	32	5.8+	0.34	0.9
	33	5.8	0.33	
	33	6.3	0.34	
	47	9.15	0.40	
	65	4.6	0.27	1.5
	65	7.1	0.35	1.1
	80	5.4	0.31	0.85
	80	6.1	0.34	1.1
θ	32	11.5	0.39	
	33	11.3	0.41	
	47	10.1	0.38	
	52	9.8	0.36	0.9
	80	8.75	0.34	
θ'	47	10.5	0.38	
	52	10.2	0.36	
	80	9.15	0.34	
μ	25	17.5	0.49	

[32] The notation is similar to that of L. P. Bouckaert, R. Smoluchowski, and E. Wigner [Phys. Rev. **50**, 58 (1936)] with the addition of Z to distinguish the tetrad axis. Note that upper-case Greek characters are used to label symmetry points while lower-case Greek characters denote families of data. No relation is implied between a family of data and the symmetry point of the same Greek character.

The extremal cross-sectional area of each surface is assumed to be a single-valued function of magnet angle; the multiplicity of branches is due to the existence of several inequivalent (i.e., not identical under inversion) sites with the same type of symmetry. The number of inequivalent sites for each type of symmetry point is equal to the number of branches in plane *A* or plane *E*, since these planes are not mirror planes in a tetragonal system. Branches in Fig. 8 which are required by symmetry to have zero slope at an axis are marked with a half-box at or near the axis. Crossings which are required to occur exactly at symmetry axes, e.g., at [111], are circled at that axis.

The over-all range of areas for any family of curves, as well as the detailed shapes of the curves, depend on the particular dimensions, shape, and orientation of the model surface chosen and may differ widely from those of Fig. 8. The connectivity, degeneracies, and occurrence of zero slopes, however, depend only on the symmetry and cannot be altered without assuming more complicated surfaces. (In constructing Fig. 8, the order of magnitude of anisotropy of the simple surfaces has been chosen so as to facilitate comparison with the data.)

Several families of data in Fig. 3 can be classified by comparison with Fig. 8. Families of data labeled ϵ, θ, and θ' have the symmetry of the point Δ, while ζ and η have symmetries of the points ΔZ and Σ, respectively.

For quantitative comparison, ellipsoids were used as the simple closed surfaces situated at the appropriate symmetry points. The areas of the principal cross sections were fitted to the data at high-symmetry points; in the case of ζ the angle of tilt was determined by the 26° displacement of the minimum from [100] in plane *C*. The frequency-versus-angle curves for the ellipsoidal models were calculated by computer and

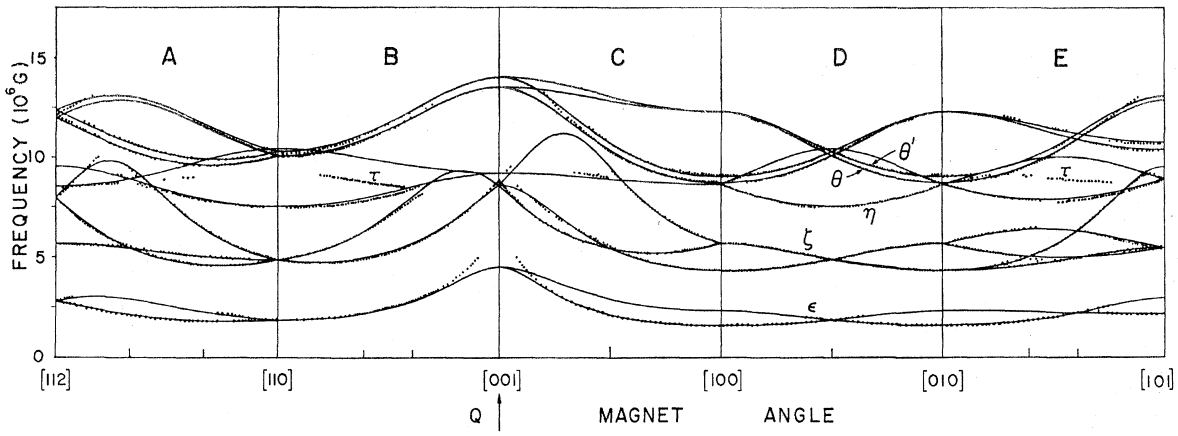

FIG. 9. Dots: five families of data from Fig. 3. Solid lines: frequency branches expected on the basis of simple ellipsoidal models with the parameters listed in Table II.

are shown as solid lines in Fig. 9 superimposed on the pertinent data. Where the data exist, the agreement is excellent—in most cases within a few percent. The only exceptions are the data labeled τ. While the branches τ are not clearly connected with the family labeled η, they are plotted here for reference in Sec. IV B. Also, we comment that the solid lines computed for ζ in plane A consist of four branches, the lower two of which are indistinguishable from each other on this scale. The near degeneracy explains the apparently single branch of data.

To find patterns in the angular range of the data, a stereogram was plotted for one ellipsoid of each family. Figure 10 is the result for ϵ and shows the range of field direction through which the data extend. The simplest interpretation of the dashed line separating the data region from the nondata region is that it defines the edge of an opening or distortion at one end (or both ends) of the longest axis of the ellipsoid, as shown by the hatched area in Fig. 11. The orientation of each member of the family of four such surfaces, located at the four symmetry points Δ, is uncertain by a 90° rotation about Q; i.e., the longest axis could lie either parallel to the $\Gamma\Delta$ line or perpendicular to it. The uncertainty is indicated by the use of angular brackets instead of square brackets. Somewhat similar results are obtained for frequencies θ and η, in Figs. 12(a) and 12(b), respectively. A stereogram for ζ (Fig. 13) shows that the data disappear only when **H** lies within a conical solid angle closely centered about the direction corresponding to the largest cross section of the ellipsoidal model. The half-angle of the cone is ~20°. Such a nondata region cannot be explained by an opening in the ellipsoid, and a more reasonable interpretation is suggested in Sec. IV B. The orientation and relative shape of the model ellipsoid for ζ without regard for the disappearance of data are shown by the principal cross sections in Fig. 14.

A simple cylindrical fit to data for the μ branch is shown by the solid line in Fig. 15, with the cylinder axis parallel to [001] and minimum cross-sectional area[33] corresponding to frequency $f_0=15.8\times10^6$ G. In

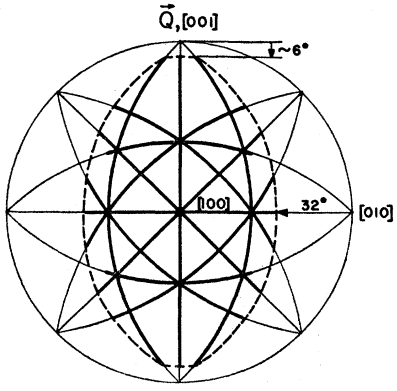

FIG. 10. Stereogram showing the angular extent of data for frequency ϵ. Heavy lines indicate the observation of data. A similar stereogram could be drawn with [100] and [010] interchanged.

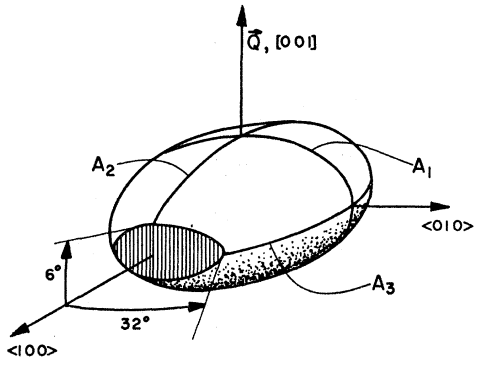

FIG. 11. Simple ellipsoid fitted to frequency ϵ. The opening in one (or both) ends is deduced from the angular extent of data in Fig. 10.

[33] We use the conversion factor frequency (10^6 G) = 104.8× area (Å^{-2}).

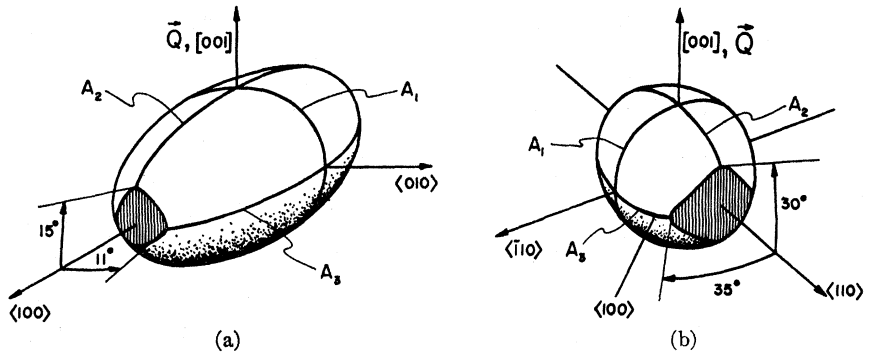

FIG. 12. Simple ellipsoids fitted to (a) frequency θ and (b) frequency η. Openings exist in one or both ends of each ellipsoid. An ellipsoid could be drawn for frequency θ' with dimensions only slightly larger than for θ (see Table II).

plane C, the data follow the curve closely out to 66° from $\mathbf{Q}$, beyond which the signal disappeared in noise. The slight departures of the data from the solid line indicate undulations in the cylinder. The intersection at [001] of two branches in plane B with one branch in plane C indicate symmetry of the point Σ. This connectivity also implies that the cylinder is not a surface of revolution. Undulations in the cylinder should give rise to two frequencies with $\mathbf{H} \parallel [001]$ that approach each other as $\mathbf{H}$ is rotated away from [001], and this may account for the weaker branch μ' in plane C. Unfortunately, μ' is too weak to be followed in plane B, due to the presence of the stronger branches μ.

The line drawn through the data labeled ν is that for a cylinder with $f_0=26.8\times10^6$ G. We tentatively classify ν as due to another cylindrical surface.

The line through the data labeled μ_2 is drawn at twice the frequency of that through μ, which suggests that μ_2 is a second harmonic of μ.

The parameters used to fit the simple geometrical models to the data are listed in Table II.

B. Superlattice Effects

We now assume a particular Fermi surface for paramagnetic Cr and investigate the orbits which result from the antiferromagnetic superlattice truncations. Lomer[8] has proposed a Fermi surface for the Cr-group metals based on Wood's augmented-plane-wave (APW) calculation for iron.[34] He suggested that the antiferromagnetism in Cr is stabilized by the fortuitous occurrence of large parallel regions of the Fermi surface. With the exception of hole pockets at N, the qualitative features of Lomer's paramagnetic Fermi surface were reproduced by the APW calculations of Loucks.[35] Figure 16 shows the results for a (100) central plane of the Brillouin zone and illustrates the nearly parallel surfaces of the hole octahedron centered at H and the electron octahedron at Γ. The characteristic wave vector of the incommensurate superlattice is $(2\pi/a)$ $(0, 0, 1-\delta)\equiv\mathbf{Q}$, which we have now taken to be along the z axis. The vector $(2\pi/a)$ $(0, 0, 1+\delta)$ differs from $-\mathbf{Q}$ by only a reciprocal lattice vector. The energy gap at the Fermi surface due to the interaction of states separated by $\pm\mathbf{Q}$ is expected to destroy most of the octahedral surfaces at Γ and H. The surface at H is larger than the one at Γ, and a large cylindrical surface might remain, but for simplicity we assume that it is entirely destroyed.

According to Lomer,[15] energy gaps should also occur in the vicinity of *any* pair of states on the Fermi surface which are separated by $\mathbf{Q}$, or in general by

$$\mathbf{q}(n)=\mathbf{G}\pm n\mathbf{Q}, \qquad n=1, 2, \cdots \tag{2}$$

where $\mathbf{G}$ is any reciprocal lattice vector. An energy gap Δ_n corresponding to $\mathbf{q}(n)$ arises in nth-order perturbation theory and is a rapidly decreasing function of n. For a given magnetic field strength, magnetic break-

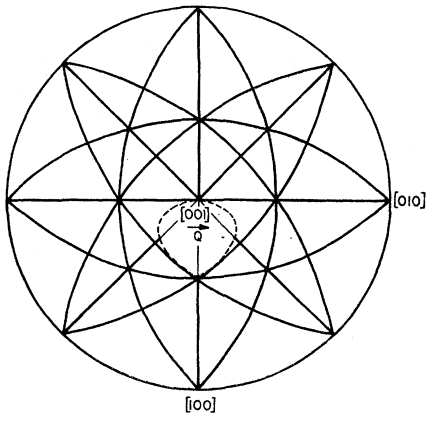

FIG. 13. Stereogram for frequency ζ. Heavy lines indicate the existence of data. A similar stereogram could be drawn with [100] and [010] interchanged.

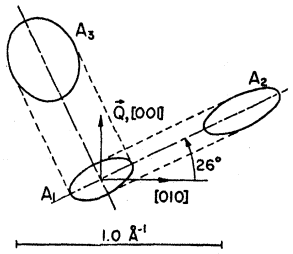

FIG. 14. Three views of the simple ellipsoid fitted to frequency ζ.

[34] J. H. Wood, Phys. Rev. **126, 517** (1962).
[35] T. L. Loucks, Phys. Rev. **139,** A133 (1965).

TABLE II. Parameters used to fit simple models to data. For definitions of areas A_1, A_2, and A_3, see Figs. 11, 12, and 14. k_i is the ellipsoid semiaxis perpendicular to A_i, A_0 is the area for **H** parallel to cylinder axis, and r_0 is the radius for a circular cylinder. Areas are given as the equivalent frequencies, in 10^6 G; linear dimensions in $Å^{-1}$.

Family of data Symmetry[a]	ϵ Δ	ζ ΔZ	η Σ	θ Δ	θ' Δ	μ Σ	ν
A_1	1.60	4.30	7.50	8.70	9.0		
A_2	2.30	5.19	10.4	12.25	12.25		
A_3	4.5	11.2	9.2	13.5	14.0		
k_1	0.140	0.203	0.197	0.240	0.241		
k_2	0.098	0.168	0.142	0.171	0.177		
k_3	0.050	0.078	0.161	0.155	0.155		
A_0						15.8	26.8
r_0						0.219	0.285

[a] See Fig. 8(b).

down should occur for all gaps above a certain order. The calculations of Falicov and Zuckermann[12] indicate that only first- and second-order gaps should be important for moderate fields, and we use this result below.

The Fermi surface shown by solid lines in Fig. 17 for paramagnetic Cr is the result of trial-and-error inspection of many shapes and sizes in an effort to interpret our dHvA data. The surface at N appears in Loucks's APW calculation for Mo and W but not in that for Cr. It could appear with a small change in potential,[36] however, and it plays a major role in the present interpretation of the dHvA data. The surface at N is an ellipsoid with semiaxes 0.173, 0.234, and 0.268 $Å^{-1}$ along NH, $N\Gamma$, and NP, respectively. Other slightly different shapes were found to give worse agreement with the data. For comparison, tic marks in Fig. 17 indicate the dimensions of this surface at N in both Mo and W, as determined by Sparlin and Marcus from dHvA data.[37] (The orientation of the two $\langle 110 \rangle$ body axes of the piece cannot be determined from dHvA data, either for Mo and W or in the present work in Cr. The orientation in Fig. 17 is drawn with the $N\Gamma$ axis greater than the NH axis, to be consistent with calculations by Lomer[8] for Cr, Loucks[35] for Mo and W, and Mattheiss[38] for W.) The shape of the electron surface at X which evolved from the present work is compared in Fig. 17 with that predicted by Loucks. It is assumed here to be a surface of revolution about ΓH.

Tetragonality in all the dHvA data implies that all Fermi-surface sheets (holes at N, electrons at X, etc.) are truncated by the superlattice. In constructing

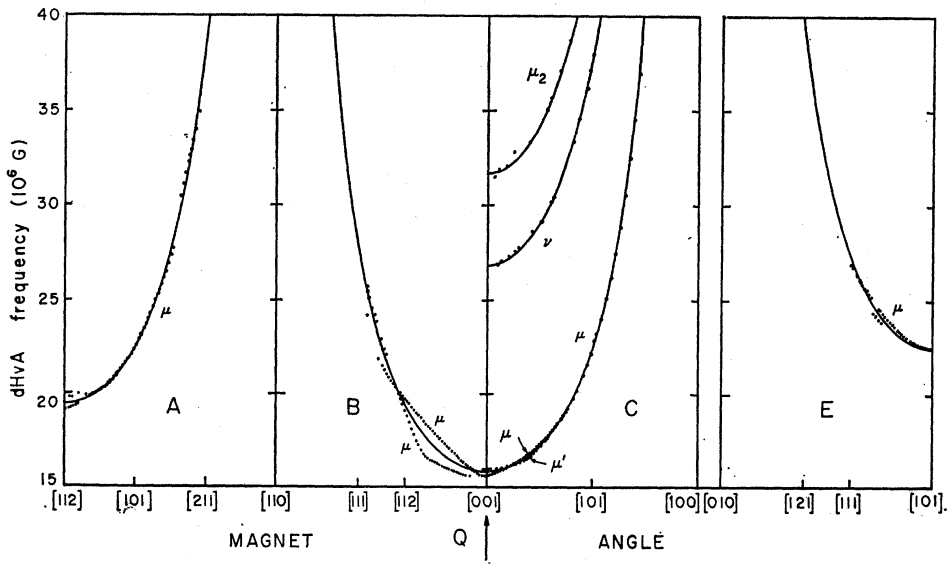

FIG. 15. Comparison of highest-frequency data and those expected from a cylinder. Parameters are listed in Table II.

[36] T. L. Loucks, Phys. Rev. **143**, 506 (1966).
[37] D. M. Sparlin and J. A. Marcus, Phys. Rev. **144**, 484 (1966).
[38] L. F. Mattheiss, Phys. Rev. **139**, A1893 (1965).

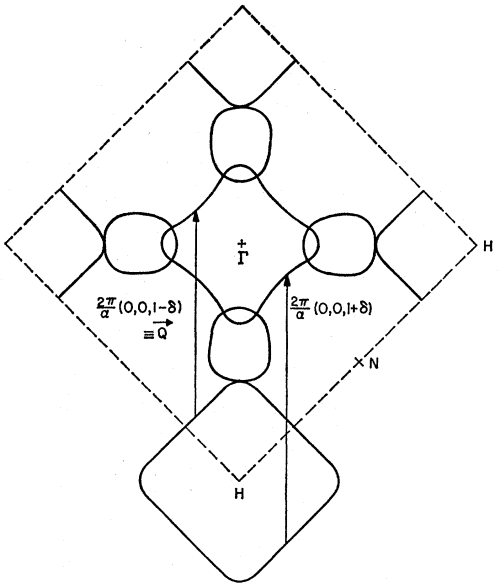

FIG. 16. Theoretical Fermi surface in the absence of magnetic ordering (after Refs. 8 and 35).

truncations, we must distinguish between N_1 and N_2, as well as X_1 and X_2 (Fig. 18). Figure 19 shows the results for the Fermi surface of Fig. 17. We choose to work in the extended zone scheme, in which case condition (2) is replaced by

$$\mathbf{q}(n)=\pm n\mathbf{Q}, \qquad n=1, 2, \cdots. \tag{3}$$

Transitions can occur between points on the Fermi surface separated by $\mathbf{q}$. The locus of such points is most easily found by translating a surface, e.g., the electron pocket at X_1, by $\mathbf{q}=\pm\mathbf{Q}$ (for first order) to obtain the dashed outlines in Fig. 19. With $\mathbf{H}$ perpendicular to the plane of the diagram, an electron on the solid orbit is allowed to make a first-order Bragg superlattice reflection to either of the dashed orbits, whichever is encountered first. The same translations by $\pm\mathbf{Q}$ are shown for the surfaces at X_2, N_1, and N_2.

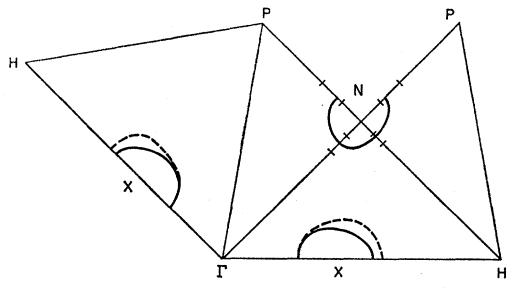

FIG. 17. Model Fermi surface assumed for Cr before truncation by the antiferromagnetism. APW results (Ref. 35) for the electron surface at X in Cr are shown by dashed lines for comparison. The tic marks about N give dimensions for the hole surface in Mo (larger) and W (smaller), determined from dHvA measurements (Ref. 37).

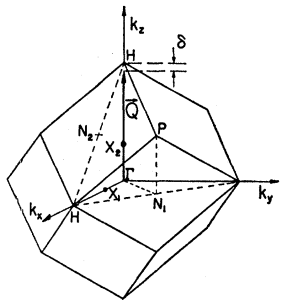

FIG. 18. First Brillouin zone for bcc lattice with tetragonal notation. The antiferromagnetic $\mathbf{Q}$ vector is also shown.

For the purpose of tracing complete orbits and including transitions to all possible orders, a long chainlike construction is very useful. The solid-dashed construction for the hole surface at N_2 of Fig. 19 has been extended into such a chain in Fig. 20. Each solid outline is translated from its nearest solid neighbor by 2δ and from its nearest dashed neighbor by δ. Thus first-order transitions occur at intersections of a solid outline with a nearest dashed neighbor, second order at intersections with a nearest solid neighbor, third order at intersections with a *next*-nearest dashed neighbor, etc. Orbits resulting from first-order transitions alone and also from first- *and* second-order transitions are shown in Fig. 20.

1 . *Holes at* N_2

Orbit (a) in Fig. 20 agrees well with cross section A_1 of the simple ellipsoid for frequency ζ, and the ΔZ symmetry of the surface is appropriate for frequency ζ. All three dimensions of the assumed hole surface at

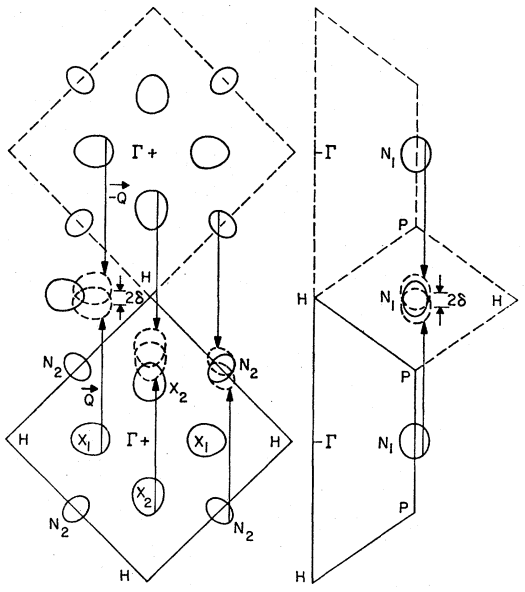

FIG. 19. Central {100} and {110} planes of the Fermi surface of Fig. 17, in the extended zone scheme, showing the location of degeneracies due to the antiferromagnetic ordering. Dashed curves represent translation of the sheets of Fermi surface by $\pm\mathbf{Q}$.

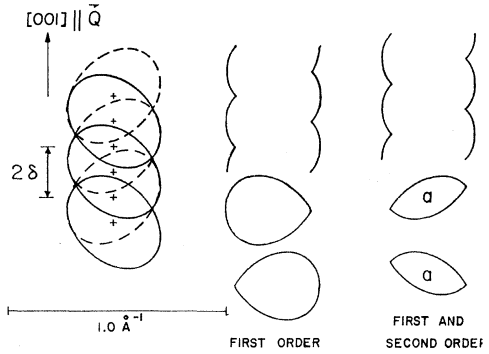

FIG. 20. Construction of orbits on the hole surface at N_2 in the (100) plane, for **H** || [100]. Orbits arising from first-order energy gaps alone are shown, as well as from both first- and second-order gaps. The figure on the left is part of an infinite chainlike figure.

N have been adjusted carefully to optimize agreement with the ellipsoidal model for ζ, and the resulting principal cross sections are shown in Fig. 21. The seam around the edge of the new surface lies in a plane because the hole pocket at N_2 has a body axis with twofold rotational symmetry that is perpendicular to **Q**. The plane is not a mirror symmetry plane for the new piece, however, and therefore the minimum area does not necessarily occur with **H** in the plane of the seam. The field direction at which the area passes through a minimum value is very sensitive to the assumed shape of the hole surface at N. The shape was adjusted to give agreement with the experimental angle of 26° from the basal plane, and also to agree with cross sections A_2 and A_3. The absence of ζ data for **H** near the direction of maximum area, as noted above and in Fig. 13, is now attributed to the relatively sharp edge which extends around the surface at the seam. When **H** is nearly perpendicular to the plane of the seam, no part of the extremal orbit is very far from the edge, so that the number of electrons participating in the dHvA effect is correspondingly low. The resulting signal is expected to be much weaker than it would be for a smooth ellipsoid. Another weakening effect is that $m^*/m_0 \approx 0.5$ (Table I), at which value spin-splitting effects[39] are expected to reduce the fundamental dHvA amplitude to zero.

2. *Holes at N_1*

With no further adjustment of the dimensions or shape of the paramagnetic hole surface at N, we are able to account for two other families of frequencies, η and μ, which we interpret as arising from N_1. The chainlike construction for N_1 is shown in Fig. 22. The dashed and solid outlines differ in shape because the assumed surface does not have fourfold symmetry about that body axis (N_1P) which is parallel to **Q**, as shown in Fig. 19. All the orbits have the symmetry of the point Σ, which according to Table II is appropriate for frequencies η and μ. Orbit (c) of Fig. 22 is formed by the dome of one pocket and the bottom of an identical pocket centered at a position 2δ higher than the center of the first. As **H** is rotated in the basal plane from ⟨110⟩ toward a ⟨100⟩ direction, the extremal area of the new piece increases slowly; at 12° past the ⟨100⟩ direction the extremal orbit begins to intersect the nearly flat face which is the result of first-order transitions. 45° past the ⟨100⟩ direction (the next ⟨110⟩ direction) the orbit is that of (b) in Fig. 22. Three principal views of this closed piece are shown by the solid outlines of Fig. 23. The dashed lines represent the simple ellipsoid for frequency η and the tic marks indicate the angular limits to which the simple ellipsoid is a good fit to the data. We now interpret the apparent opening or distortion in the ends of the simple ellipsoid, Fig. 12(b), as being due to nearly flat faces which cause a decrease in area from that expected of the simple ellipsoid. The angular variation of extremal area is probably quite small for orbits which cross this flat face, so that the dHvA torque oscillations would be weak. The frequency branches labeled τ in planes B and E of Fig. 3 vary slowly with angle and are 10–15% smaller than the branches that one would expect for simple ellipsoids fitted to η (Fig. 9). We associate them tentatively with the family η and assign both η and τ to the flat-faced piece of Fermi surface in Fig. 23. We point out, however, that at no place in the data is there a clear connection between the branches τ and branches of the family η. In regions where one might expect a connection, the amplitude of τ is very weak or there are close-lying frequencies from other families of data which confuse the picture. We assume that the small or zero amplitude of the torque oscillations in those regions is due to the area passing through a relative maximum as the orbit begins to intersect the flat face.

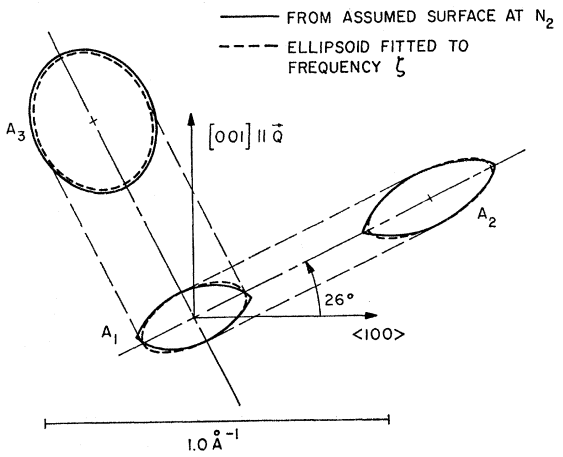

FIG. 21. Orbits on a surface formed by second-order energy gaps from the hole surface at N_2 [orbit (a) of Fig. 20], compared with the simple ellipsoid fitted to frequency ζ (Fig. 14).

[39] M. H. Cohen and E. I. Blount, Phil. Mag. **5**, 115 (1960).

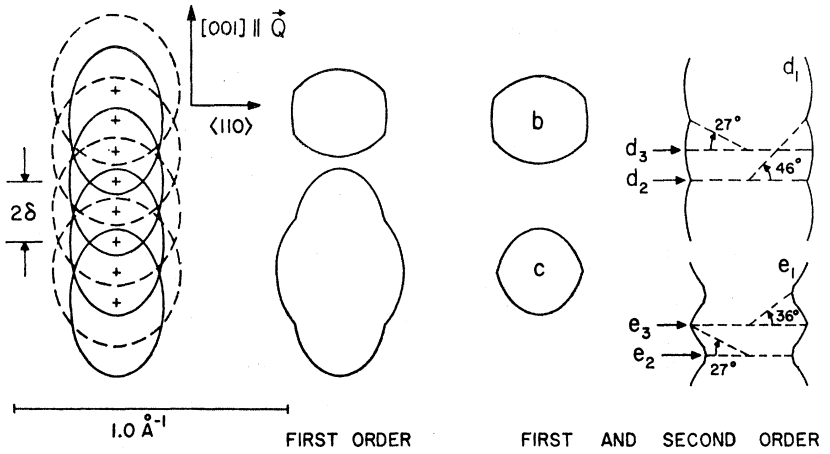

FIG. 22. Construction of orbits in a (110)-type plane that arise on the hole surface at N_1. Energy gaps to second order are considered.

The agreement between dashed and solid lines in Fig. 23 is excellent for all regions away from the flat face. We emphasize that the solid outlines were obtained from the assumed hole surface at N in paramagnetic Cr without further adjustment than was necessary for optimizing agreement with frequency ζ.

Considering other orbits which arise from the hole surface at N_1, we find good agreement between orbits labeled (d) in Fig. 22 and frequency μ. Orbit (d_1) is along the outside of the undulating cylinder in Fig. 22; it exists only if both first- and second-order transitions occur. A three-dimensional view of the construction (Fig. 24) illustrates the undulations. Orbit (d_2) occurs with $\mathbf{H} \parallel [001] \parallel \mathbf{Q}$, and is identical to orbit (d_3) after rotation about $\mathbf{Q}$ by 90°. As $\mathbf{H}$ is rotated toward [110], the area of (d_2) increases more rapidly with angle than for a cylinder, while the area of (d_3) increases more slowly than for a cylinder. The angle from [001] at which the area of (d_3) begins to rise more steeply is estimated from Fig. 22 to be 27°. Orbit (d_2), on the other hand, initially rises more steeply, then less steeply than a cylinder until ~46°, where it again rises suddenly. These angles in the model are determined only by the orbit diameter and the magnitude of δ. The data in plane B of Fig. 15 exhibit almost exactly this behavior. The two branches of μ weave back and forth across the curve for a cylinder; the lower branch near [001] has a sudden change in slope at ~26° while the upper branch increases smoothly until ~46°, where it undergoes a sudden increase. In plane B, the data were lost in noise past ~52° from [001]; in the other planes the data could be followed over greater angular ranges and are consistent with the foregoing interpretation. By symmetry, orbit (d_4), which is located half-way between (d_2) and (d_3) in Fig. 24, must also be an extremal. If orbit (d_2) is a minimum area with respect to $\mathbf{k}_H$, then (d_4) must be a maximum, and vice versa. If the surface at N is even only roughly ellipsoidal, one would expect (d_2) and (d_3) to be the minimum. The area of (d_4) should approach that of (d_2) as $\mathbf{H}$ is rotated away from [001]. The required angular behavior is exhibited by μ' as far as it can be followed, and its identification as orbit (d_4) seems reasonable.

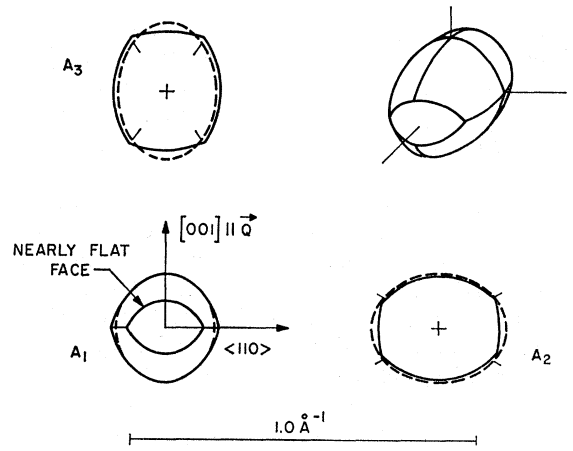

FIG. 23. A surface formed by first- and second-order energy gaps from the hole surface at N_1 [orbits (b) and (c) of Fig. 22], compared with the ellipsoid fitted to frequency η [Fig. 12 (b)].

The area of orbit (d_3) in Fig. 24 was measured by planimeter and corresponds to a frequency of 14.4×10^6 G, which is ~9% less than the value of μ at [001]. Planimeter measurement of orbit (d_4) in Fig. 24 yields a slightly larger frequency, 14.5×10^6 G, which is within ~10% of 16.0×10^6 G for frequency μ' at [001]. These indicate roughly a 5% discrepancy in radial dimension of the cylinder. The arguments of symmetry and the close correspondence of special angles and dimensions seem to be good evidence in support of our interpretation of frequencies μ and μ'.

No clear evidence was found for the cylindrical surface (e) in Fig. 22. Because of complexity in the data near [001], the connectivity of ρ and φ (Fig. 3) has not been established. If they were found to have the symmetry of Σ or Z they might be interpreted as orbit (e_2) or (e_3), especially since frequency φ in plane B

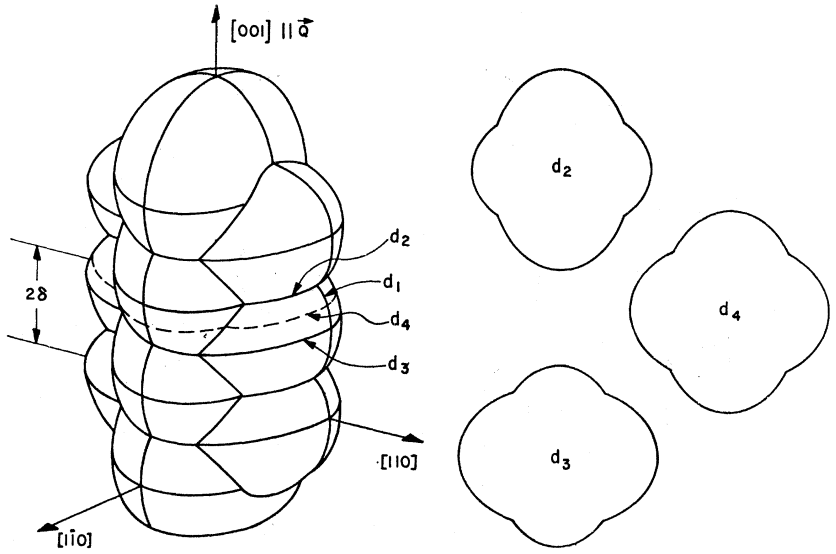

FIG. 24. Part of the infinite chain-like surface formed by first- and second-order energy gaps from the hole surface at N_1 [orbit (d) in Fig. 22].

exhibits a sudden change in slope at ~28° from [001], as required for orbit (e_2) in Fig. 22.

3. *Electrons at X_1*

The electron surface at X_1 provides a possible explanation of frequency θ. Figure 25 gives the construction and orbits for **H** || [010]. All orbits are open for this orientation of **H**, but the region (f) in second order is a cavelike structure which supports closed orbits when **H** has been rotated away from [010]. Assuming that the electron surface at X is a surface of rotation about the ΓH line, we can estimate the shape of the cave. Figure 26 shows the results compared with the ellipsoid which was fitted to frequency θ. The agreement is fairly good and would be improved by the rounding of edges expected at truncations. The angle of disappearance of an extremal cross section in the non-centrosymmetric cave is difficult to estimate but may be near the experimentally determined angles indicated by tic marks.

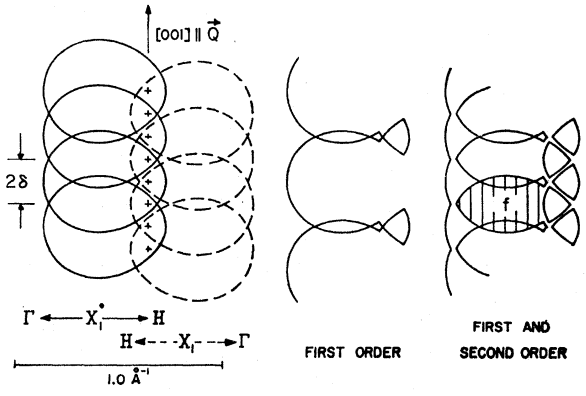

FIG. 25. Construction of orbits on the electron surface at X_1 in the (100) plane for **H** || [100].

4. *Electrons at X_2*

Figure 27 for electrons at X_2 offers no clear explanation of data. None of the data has the symmetry of the point Γ as required for orbits (g), (h), and (n). Orbit (k) may be responsible for the sharply rising short branches κ near the center of plane C, in the range $10\text{–}20\times10^6$ G. Orbit (m) is on a less sharply undulating cylinder of larger minimum cross section, and may be responsible for frequency ν. The angular variation of ν must be better established before a more definite interpretation can be made.

V. CONCLUSIONS

A Fermi surface consisting of hole ellipsoids at N and electron pockets at X was assumed for paramagnetic Cr. Superlattice truncation of this surface in the manner suggested by Lomer produces a Fermi surface of tetragonal rather than cubic symmetry. Assuming only first- and second-order truncations to be important, orbits can be found on this truncated Fermi surface that provide a semiquantitative explanation for several families of data. In this interpretation, the hole ellipsoids at N are responsible for at least three families of data: η, ζ, and μ. The interpretation includes open orbits in the direction of **Q**, as predicted by Lomer and observed in magnetoresistance data.[23] The dimensions of the untruncated ellipsoids at N were adjusted so that, after truncation, the various orbit areas agreed with the three families of data to ~10% or better.

Frequency θ is tentatively identified with a "cave"

orbit due to the electron pocket at X_1. The orbit agrees with the data to ~20% but does not account for the existence of θ', which appears as a doublet with θ over a large angular range. The presence of other doublets and even triplets of frequency branches remains unexplained.

Frequency ϵ is due to an ellipsoidal piece of Fermi surface with a well-defined opening in one or both ends.

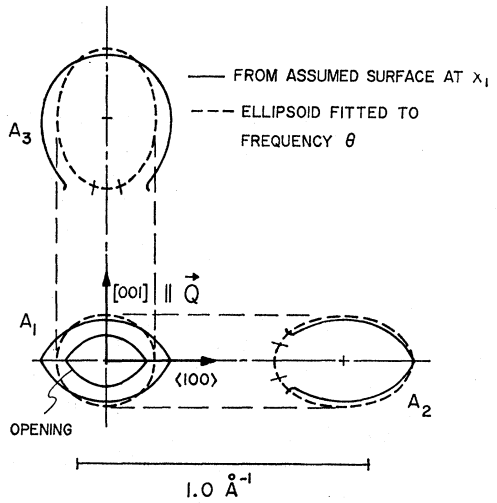

FIG. 26. Three views of the "cave" surface formed by first- and second-order energy gaps from the electron surface at X_1 [region (f) in Fig. 25], compared with the simple ellipsoid fitted to frequency θ [Fig. 12 (a)]. The tic marks on the simple ellipsoid mark the opening deduced from the disappearance of data at certain field directions.

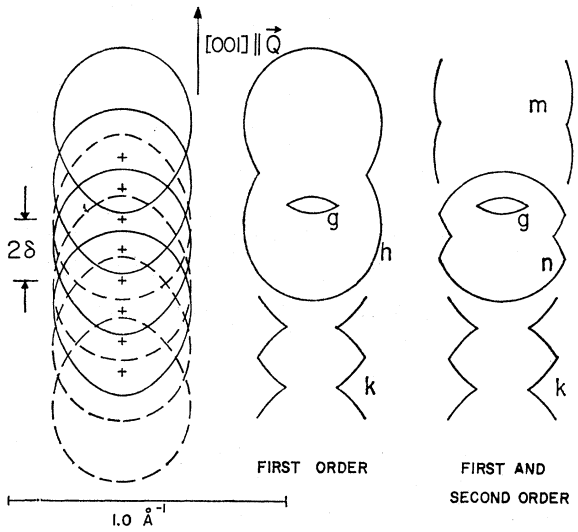

FIG. 27. Construction of orbits on the electron surface at X_2, for **H** in a ⟨100⟩ direction.

The symmetry of ϵ suggests that it arises from the electron pockets at X_1 or the hole ellipsoids at N_2, but we have no more specific interpretation.

ACKNOWLEDGMENTS

We are grateful to L. M. Falicov and M. J. Zuckermann for a number of very fruitful discussions. The comments of A. J. Arko and R. A. Montalvo are appreciated, and we thank J. H. Condon for helpful criticism during preparation of the final manuscript.